Synthesis, characterization, and azo dye degradation performance of mechanically alloyed $Mg_{65}Cu_{20}Y_{13}La_2$ nanocrystalline powders

Nilüfer Danacı[1,*] , Musa Göğebakan[2], Hakan Yaykaşlı[3,4], Celal Kurşun[2], and Serhan Uruş[5]

[1] Department of Materials Science and Engineering, Kahramanmaraş Sütçü İmam University, Kahramanmaraş, Turkey

[2] Department of Physics, Faculty of Sciences, Kahramanmaraş Sütçü İmam University, Kahramanmaraş, Turkey

[3] Department of Property Protection and Safety, Elbistan Vocational School of Higher Education, Kahramanmaraş İstiklal University, Kahramanmaraş, Turkey

[4] Department of Material Science and Engineering, Institute of Graduate Studies, , Kahramanmaraş İstiklal University, Kahramanmaraş, Turkey

[5] Department of Chemistry, Faculty of Sciences, Kahramanmaraş Sütçü İmam University, Kahramanmaraş, Turkey

ABSTRACT

This research describes the synthesis of the multicomponent $Mg_{65}Cu_{20}Y_{13}La_2$ alloy by mechanical alloying (MA) to investigate the influence of milling times on the microstructure of alloy and degradation performance of methyl orange. The structural evolution of this alloy was investigated by using X-ray diffraction (XRD), scanning electron microscopy (SEM), and energy-dispersive spectrometry (EDX) techniques. The thermal behavior of the alloys was investigated by differential scanning calorimetry (DSC). The crystallite size of the $Mg_{65}Cu_{20}Y_{13}La_2$ alloys was calculated using the Debye Scherrer equation with broadening of the XRD peaks. The methyl orange degradation efficiencies of the $Mg_{65}Cu_{20}Y_{13}La_2$ alloys were evaluated by using ultraviolet–visible (UV–Vis) spectroscopy, Fourier-transform infrared spectroscopy (FT-IR), and gas chromatography–mass spectrometry (GC–MS) techniques. The XRD and SEM results showed that the microstructure of the powders changed during MA. After 10 h milling time, three intermetallic phases were obtained as Mg_2Cu_2La, $Mg_{24}Y_5$, and Mg_2Cu. The results also showed that a solid solution phase, α-Mg(Cu, Y, La), with an average crystallite size 21 nm was formed after 100 h milling time. DSC trace of the $Mg_{65}Cu_{20}Y_{13}La_2$ powders showed two exothermic peaks for the 10 h milling time, while it did not show any peaks for the 100 h milling time. Photocatalytic decomposition of the methyl orange solution by the $Mg_{65}Cu_{20}Y_{13}La_2$ alloy was evaluated by UV–Vis spectra with a decrease in absorbance at a wavelength of 465 nm. After a 20 min exposure, UV–Vis, FT-IR, and GC–MS analysis showed that the methyl orange samples were almost completely degradation by using the $Mg_{65}Cu_{20}Y_{13}La_2$ powders. The $Mg_{65}Cu_{20}Y_{13}La_2$ alloy exhibits a good reusability of 92% by the four cycle and a

Address correspondence to E-mail: nilufer46danaci@hotmail.com

Springer

high efficiency was achieved in all the pH values in the range of 5–9. The results prove that the $Mg_{65}Cu_{20}Y_{13}La_2$ alloy is an efficient and promising material for dyeing wastewater treatment.

1 Introduction

Azo dyes are widely used in the textile industry. Some azo dyes and their decolorized products have a carcinogenic effect. Thus, it is necessary to apply efficient treatment methods to remove azo dye pollution from wastewater [1]. Many methods, such as biological treatment, chemical treatment, physical treatment, advanced oxidation processes, coagulation, and flocculation are used to remove azo dyes from wastewater. However, these methods have some disadvantages such as waste sludge formation, high cost, and difficulties in application [2]. Among other methods and materials, the most widely used azo dye degradation technology is the use of zero-valent metals (ZVM). One of the most studied materials for this purpose is zero-valent iron (ZVI), which provides good azo dye degradation efficiency [3–5]. Researches focuses on the production of new intermetallic phases with a metastable structure to improve the efficiency of the degradation mechanism. The aim of researches is to increase the reactivity by combining different metallic elements. Another aim is to increase the specific surface area by producing nanoparticles. The mechanical and physical properties of a material vary depending on the microstructure of that material. For the industrial use of a material, the identification of the microstructure of that material is very important from an engineering point of view. Since the properties of pure metals are same, they naturally have a single-phase structure. But, there is a multiphase structure in alloys formed as a result of combining more than one element. The microstructure of an alloy can be changed depending on the chemical content of the alloy elements, temperature, and cooling rate. MA is a simple and effective method to produce metallic nanocrystalline or amorphous materials. This method provides mechanical energy to produce new intermetallic phases or solid solution phases that increase the diffusion of the initial components. Moreover, mechanically alloyed powders show metastable nanocrystalline or amorphous structures

with rough surfaces [6, 7]. Researches have shown that some amorphous and nanocrystalline alloys provide more effective results in dye removal from wastewater than the corresponding crystalline alloys or ZVM. For this purpose, many alloys such as Fe-based [8–10], Mg-based [2, 11], Al-based [12], and Co-based [13, 14] have been produced by using various methods. Researches proved that the methyl orange degradation performance by using Fe–Si–B amorphous alloy is 1000 times higher than nano-ZVI powders [14, 15]. Fe-based amorphous alloys have high azo dye removal efficiency, but its corrosion products reduce the rate of subsequent degradation [14, 16]. Although Cu-based alloys have better corrosion resistance than Fe-based alloys, their applicable pH value range is limited [14, 17]. Tang et al. [14] reported that amorphous Co-based alloy on the degradation of Direct Blue 6 azo dye had a high degradation performance within 2 min with a degradation efficiency of 99% and reusability with over 20 cycles. Ma et al. [1] proved that the methylene blue degradation efficiency of amorphous alloys has reached 99% within 5 min and it is understood that the surface morphology of the amorphous alloys is very effective on the degradation performance. Ji et al. [18] reported that the amorphous Fe-based alloy showed promising results in Orange II degradation within a short time, and the dye degradation efficiency of the Fe-based alloy reached 99% within 70 min. Wang et al. [11] showed that the azo dye degradation reaction activity by using Mg-based metallic glass powders was 20 times more than crystalline magnesium alloy powders. Kurşun et al. [19] demonstrated that the mechanically alloyed Mg-based nanostructured powders have well degradation performance without using any extra processes such as oxidants, heat, or light sources.

Among the advanced alloy systems used for the purpose of dye degradation, Mg-based alloys exhibit a high degradation efficiency when they react with the dye solution. However, the high corrosion rate of crystalline elemental magnesium during decomposition

causes a decrease on the degradation efficiency of dye and lifetime of the alloy [20]. As a result, the development of new Mg-based alloy materials with enough lifetime, wide applicable pH range in the dye degradation, and their use in the field of wastewater treatment is the focus of this research.

In this work, the $Mg_{65}Cu_{20}Y_{13}La_2$ alloy was synthesized by using the MA method. The structure, phase analysis, thermal analysis, and morphological features of the $Mg_{65}Cu_{20}Y_{13}La_2$ alloys were characterized by using XRD, SEM, EDX, and DSC. Also, the effect of the $Mg_{65}Cu_{20}Y_{13}La_2$ alloy on the degradation performance of the methyl orange was investigated by using UV–Vis, FT-IR, and GC–MS.

2 Methods and materials

2.1 Preparation and analysis of the $Mg_{65}Cu_{20}Y_{13}La_2$ alloys

In this study, quaternary Mg–Cu–Y–La powder alloys with the nominal composition (as atomic percent of the $Mg_{65}Cu_{20}Y_{13}La_2$ alloy) was mechanically alloyed in planetary ball mills (Fritsch Pulverisette 5). The high purity Mg(99.9%), Cu(99.7%), Y(99.8%), and La(99.9%) elemental powders were weighed in specific quantities according to the desired composition under the argon atmosphere in room temperature. Powders and stainless steel milling balls (3 mm and 8 mm in diameter) were charged into a stainless steel vial (125 ml). The ball to powder ratio (BPR) was maintained as 15:1. 1% of stearic acid was added to prevent agglomeration of the powders. The mechanical alloying was performed at the rotation speed of 300 rpm. The process was interrupted for 20 min after each 20 min of ball milling. The powders were milled during 100 h and were taken at certain time intervals as 0, 10, 40, 50, and 100 h. The microstructural evaluation, phase transformations, and crystallite size evolution of the $Mg_{65}Cu_{20}Y_{13}La_2$ alloys were analyzed by XRD (by using a Philips X'Pert Pro diffractometer with Cu-K$_\alpha$ radiation in the 2θ range of 20°–90° at 30 mA and 40 kV). SEM (by

using JEOL JCM 5000 scanning electron microscope at an acceleration voltage of 10 kV) was performed to evaluate the morphology of milled powders and EDX analysis was used for structural analysis of the $Mg_{65}Cu_{20}Y_{13}La_2$ alloy. Thermal behavior of the alloyed powders was analyzed by DSC (by using Perkin Elmer Sapphire at 40 ℃ min^{-1} heating rate under a flowing nitrogen atmosphere).

2.2 Dye degradation

The methyl orange, a very commonly used azo dye, was selected to study the photocatalytic decomposition by the $Mg_{65}Cu_{20}Y_{13}La_2$ alloy. The light source used for the present photocatalytic decomposition is daylight. Daylight is the combination of all direct or indirect sunlight during the daytime. It is thought that the intensity of sunlight emitted only from windows in a closed area is average 5000 lux in the midday. Light is an important parameter affecting the dye decomposition mechanism. The number of electrons emitted by the metal depends on the intensity of the incident light. The number of photoelectrons increases directly proportional to the intensity of the incident light. The chemical characteristics of the methyl orange are given in Table 1. The methyl orange solutions prepared with distilled water were used for degradation experiments. The dye sample concentration was selected as 100 ppm (mg l^{-1}) for each experiment. A certain amount of the methyl orange was added to 100 ml of distilled water, and the pH of the samples was adjusted by using diluted 0.1 M HCl and 0.1 M NaOH. Then, 0.01 g of alloy was added to each sample and kept in a dark environment for 15 min. Finally, a certain amount of boron hydride ($NaBH_4$, reducing reagent, 0.1 g) was added to the sample solutions. The pH of the dye solution was 6, and all experiments except pH experiments were conducted at this pH value. Samples were stirred for 2 min by means of the mechanical stirrer at a fixed speed of 800 rpm, rested for certain periods of time, and filtered. The dye degradation efficiencies of the alloys were analyzed with UV–Vis spectroscopy (Shimadzu-1800). Initially, a control sample

Table 1 Chemical characteristics of the methyl orange azo dye [21]

Product	Formula	Molecular mass (g mole^{-1})	pH	λ_{max}	Color
Methyl orange	$C_{14}H_{14}N_3NaO_3S$	327.34	2.3 (acidic)	504	Red
Methyl orange	$C_{14}H_{14}N_3NaO_3S$	327.34	9.8 (alkaline)	470	Yellow

(dye-distilled water) was scanned in the 300–600 nm range with 1-nm intervals. The maximum absorbance peak appeared at 465 nm wavelength, and each sample's absorbances were collected at this wavelength.

In addition, the reusability of the $Mg_{65}Cu_{20}Y_{13}La_2$ catalyst for the purpose of the methyl orange decomposition was tested; firstly, the alloy-dye solution was dried in the oven, then it was washed with the excess amount of ethanol: water solution; finally, it was dried again and separated. The purified alloy was used again and again.

After the photocatalytic degradation tests, the catalyst was evaluated as morphological by using SEM and X-ray photoelectron spectroscopy (XPS) after drying in the oven at 70 °C. In addition, the liquid phase after the catalysis reaction was examined with FT-IR after drying the liquid phase in the oven at 70 °C. The organic degradation products in the oily sample obtained from the dried liquid phase were extracted with ethanol (absolute) and injected into Perkin Elmer Clarus 600 GC–MS Electron Impact (70 eV) (with an Elite 5-MS capillary column, 60 m × 0.25 mm × 0.25 μm i.d.). Helium (> 99.99%) was the carrier gas at a constant flow rate of 1.0 ml min^{-1}. The extracted sample's injection volume and injector temperature were 1 μl in a 10:1 split ratio and 240 °C, respectively. The oven temperature program was firstly held at 40 °C for 3 min, and subsequently, it was heated to 100 °C at 4 °C min^{-1} (held for 1 min.), and then it was increased to 180 °C at 4 °C min^{-1} (held for 8 min), and finally it was heated to 240 °C at 4 °C min^{-1} (held for 3 min.). The process parameters of the mass spectrophotometer are as follows: solvent delay, electron impact ionization mode, transfer line temperature, and ion source temperature were 0–5 min, 70 eV, 290 °C, and 270 °C, respectively. Also, the mass scan range, scan time, and interscan delay were 30–700 (m/z), 0.2, and 0.1 s, respectively.

The daylight increases the reductive degradation of the methyl orange in the catalysis system using tetrahydroborate as a co-factor. When tetrahydroborate anions did not use as a co-factor in the reductive decomposition reaction, the catalysis reaction did not enough run in present studied experiments. First, $NaBH_4$ and the methyl orange are absorbed on the nanocatalyst surface. Then, electron transfer from $NaBH_4$, which acts as an electron donor to the dye, occurs on the catalyst surface. Thus, electron transfer causes the hydrogenation and degradation of the methyl orange. According to the present results,

the possible degradation mechanism of the methyl orange, the electrons in the valence band in the $Mg_{65}Cu_{20}Y_{13}La_2$ alloy may be excited to the conduction band in daylight, and the positive holes remain in the valence band on the surface of the alloy. The negatively charged tetrahydroborate anions (electron donor) may diffuse electrostatically on the alloy's surface and transfer the electrons to the conduction band of the alloy. Thus, electron transportation from the catalyst surface to the dye molecule (acceptor) is highly accelerated with the electronic cycle in the catalysis mechanism. The possible mechanism of degradation of the methyl orange by using the $Mg_{65}Cu_{20}Y_{13}La_2$ alloy is shown in Fig. 1. Here, the number of electrons emitted by the metal depends on the intensity of the incident light. That is, the number of photoelectrons increases directly proportional to the intensity of the incident light. In addition, the increase in the number of photoelectrons with the increase of the intensity of light indicates that we should associate the light intensity with the number of photons arriving at a point per unit time [33]. As a result, the electron transportation from the alloy accelerated as an electronic cycle with tetrahydroborate anions spontaneously in daylight causes degradation of the dye in water samples. The experimental results in [30] appear to be consistent with present observations.

3 Results and discussion

3.1 Microstructural evaluation

In the current study, the nanostructured $Mg_{65}Cu_{20}Y_{13}La_2$ alloys were prepared by MA method. To investigate the microstructural evaluation and phase identification of the alloy powders produced during MA, the powders were firstly examined by using XRD. XRD patterns of investigated the $Mg_{65}Cu_{20}Y_{13}La_2$ powders for as-received (0 h) and after different milling time intervals (10, 40, 50, and 100 h) are presented in Fig. 2. As seen in Fig. 2, the diffraction peak of the as-received powders consists of pure crystalline Mg, Cu, Y, and La elements, as expected. By increasing the milling time to 10 h, the peak intensities decreased and broadened due to the increase in the powder elements' internal lattice strain [19]. At this stage of the milling time (10 h), the new reflection peaks were also observed. The new reflection peaks were identified as $Mg_{24}Y_5$, Mg_2Cu by [22,

Fig. 1 Schematic illustration of the possible mechanism of photocatalytic degradation of the methyl orange by using the $Mg_{65}Cu_{20}Y_{13}La_2$ alloy milled for 50 h
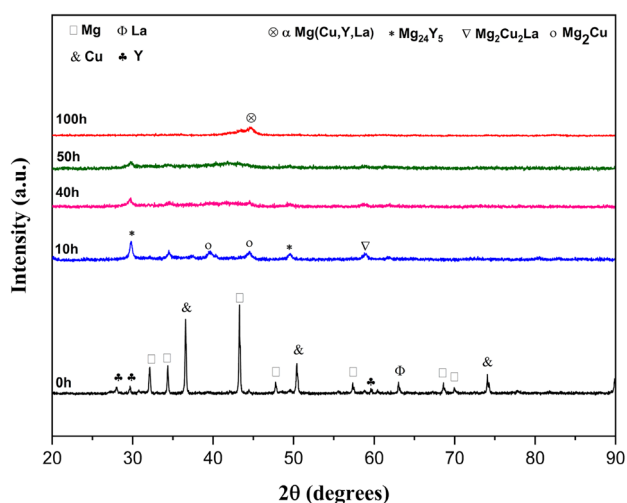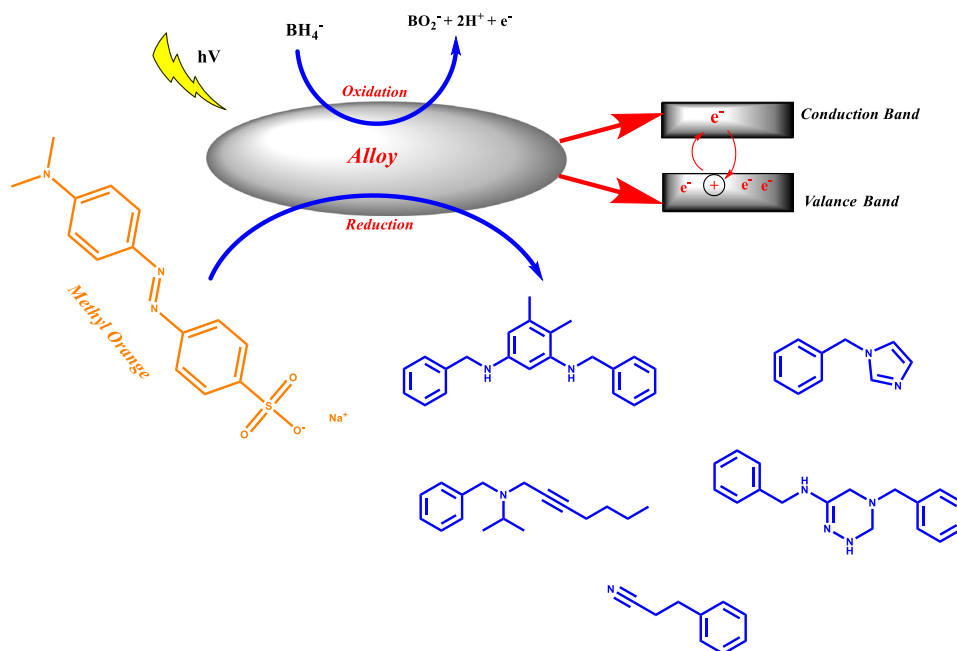

Fig. 2 X-ray diffraction patterns of the $Mg_{65}Cu_{20}Y_{13}La_2$ alloy as a function of milling time

23] and Mg_2Cu_2La intermetallic phase. Despite the very small amount of La, the observation of an intermetallic phase containing La is probably related to the limited solid solubility of La in Mg, Cu, and Y [19]. However, with increasing to 40 h and 50 h of milling time, most of the elemental peaks have disappeared. With increasing the milling time to 100 h, a broad peak corresponding to the solid solution α-Mg(Cu, Y, La) phase appeared in the 2θ range of 40°–46°. When the milling time increased to 100 h, the peak intensity of the intermetallic phases decreased and only the

predominated nanocrystalline phase of the powder alloy existed.

The crystallite size of the $Mg_{65}Cu_{20}Y_{13}La_2$ powders was calculated by using the Debye Scherrer Eq. 1 [24].

$$D = \frac{0.9\lambda}{\beta \cos \theta} \tag{1}$$

where D is the average crystallite size, λ is the wavelength of using X-ray, β is the full width (in radians) at half-maximum intensity, and θ is the diffraction Bragg angle.

The crystallite size change with milling time of the $Mg_{65}Cu_{20}Y_{13}La_2$ powders is seen in Fig. 3. As seen in Fig. 3, the crystallite size of the $Mg_{65}Cu_{20}Y_{13}La_2$ powders was obtained as 84 nm after 10 h milling time. As the milling time of 50 h, the $Mg_{65}Cu_{20}Y_{13}La_2$ powders' crystallite size decreases to the value of 21 nm. The $Mg_{65}Cu_{20}Y_{13}La_2$ powders' crystallite size remains stable after 50 h of milling. The reason of this is probably dynamic recrystallization that occurs with local heating after the alloying process. It confirms that the formation and extinction rate of dislocations becomes identical [25, 26].

The properties of nanocrystalline alloys strongly depend on microstructure and morphological features. Therefore, the samples were also examined by using SEM to investigate the influence of milling time on the microstructural features and morphological changes for the mechanically alloyed $Mg_{65}Cu_{20}Y_{13}La_2$
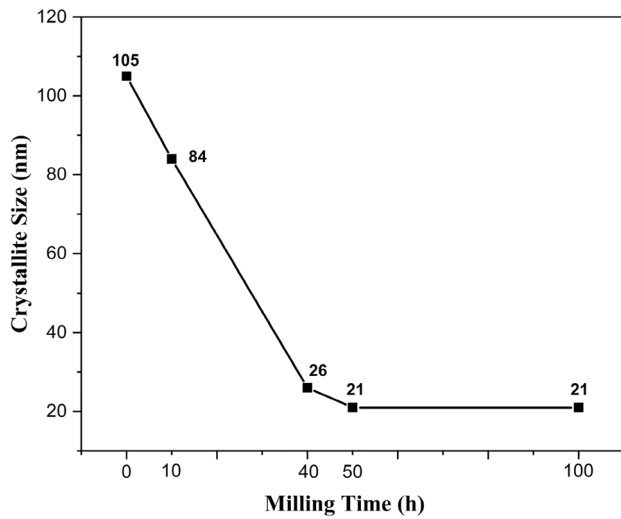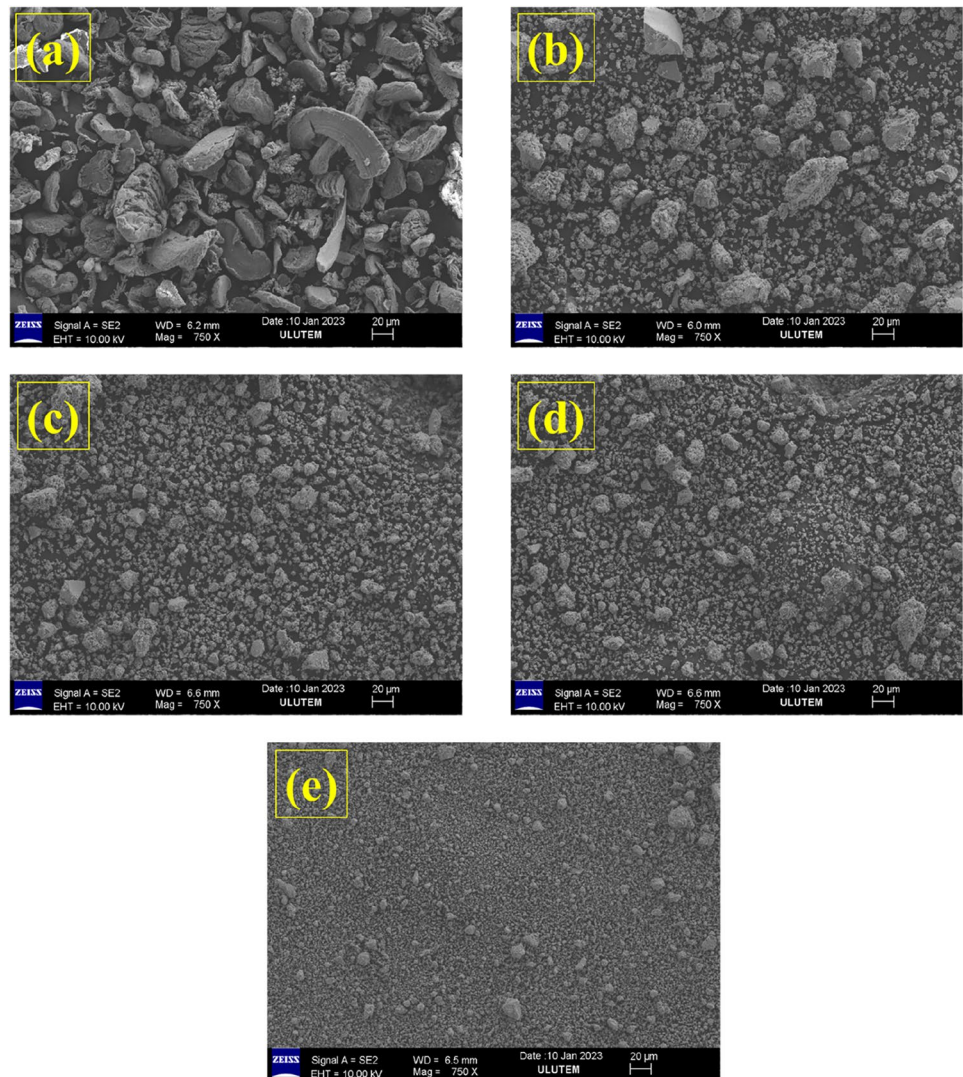
Fig. 3 The crystallite size of the $Mg_{65}Cu_{20}Y_{13}La_2$ alloy as a function of milling time

powders in more detail. The SEM micrographs for the $Mg_{65}Cu_{20}Y_{13}La_2$ powders with different milling durations are illustrated in Fig. 4. The microstructures of the as-received powder consist of pure crystalline of Mg, Cu, Y, and La elements with different size, distribution, and shapes (Fig. 4a). As shown in Fig. 4b, with the increase of milling to 10 h, the average particle size is decreased and led to the forming of agglomerates. After 40 h and 50 h of milling, larger particles undergo deformation due to the cold welding and fracturing of the particles. Particles become nearly spherical and the size is uniform, as depicted in Fig. 4c and d. After 100 h of milling, the particle sizes of the powders decreased to averaged 1 μm and the particle distribution became more homogeneous and uniform (Fig. 4e). Similar observations were concluded in the previous studies [25, 27–29].

Fig. 4 SEM images of the $Mg_{65}Cu_{20}Y_{13}La_2$ alloy as a function of the milling time: **a** 0 h, **b** 10 h, **c** 40 h, **d** 50 h, and **e** 100 h

In metastable materials, homogeneity is an important parameter affecting their application performance [19]. The EDX analysis was applied to determine the compositional homogeneity of the $Mg_{65}Cu_{20}Y_{13}La_2$ alloy. The EDX analysis of the $Mg_{65}Cu_{20}Y_{13}La_2$ alloy for 100 h of milling time is shown in Fig. 5. As seen in Fig. 5, Mg, Cu, Y, and La elements are present in the $Mg_{65}Cu_{20}Y_{13}La_2$ alloy and the $Mg_{65}Cu_{20}Y_{13}La_2$ alloy's composition is close to the as-received powder mixture. This shows that there is not much element loss during the MA process. However, the peak in 0.3 keV may be a carbon peak caused by the adhesive plate used during the analysis and the peak in 0.5 keV may be the oxygen peak caused by oxidation caused by the contact of the sample with air.

3.2 The thermal analysis of $Mg_{65}Cu_{20}Y_{13}La_2$ alloys

Thermal stability analysis of the nanocrystalline phases is critical in technological applications [25]. Phase transformations in alloys are determined by the DSC curves. Thermal properties of the $Mg_{65}Cu_{20}Y_{13}La_2$ powders for as-received (0 h) and after different milling times (10 h, 50 h, and 100 h) were examined by the DSC (Fig. 6). The DSC analyses of the samples were performed at a heating rate of 40 °C from 200 °C to 700 °C under N_2 gas atmosphere. The DSC trace of the as-received powders (0 h) showed an exothermic peak at about 356 °C and an endothermic peak at about 630 °C. These exothermic and endothermic
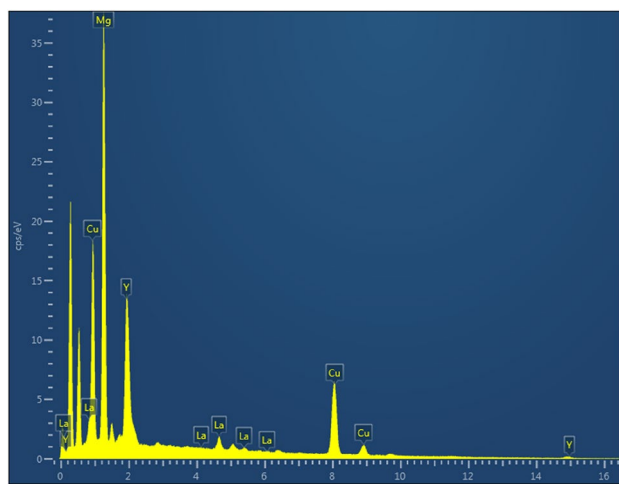

Fig. 5 EDX analysis spectrum of the $Mg_{65}Cu_{20}Y_{13}La_2$ alloy for 100 h milling time

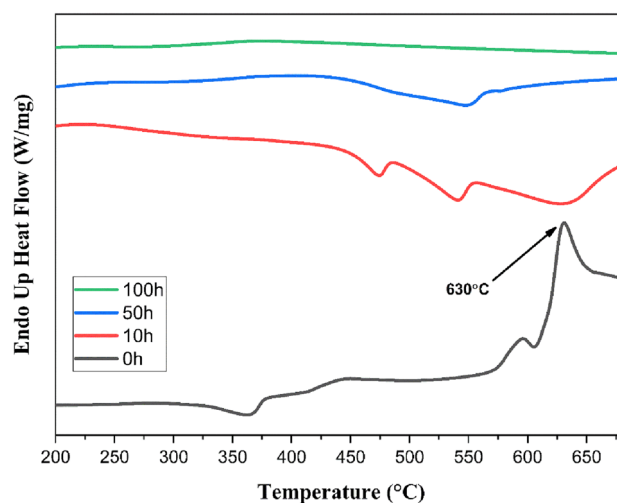**Fig. 6** DSC scans of the $Mg_{65}Cu_{20}Y_{13}La_2$ powders for 0 h, 10 h, 50 h, and 100 h

peaks may be because of the transformed FCC (face-centered cubic) structure of La element at 310 °C and the melted Mg element, respectively. The DSC trace of the $Mg_{65}Cu_{20}Y_{13}La_2$ powders after the 10 h of milling showed two exothermic peaks at around 472 °C and 539 °C. It is thought that the peak at 472 °C may be due to the formation of $Mg_{24}Y_5$ phase [23] and the peak at 539 °C may be due to the formation of the Mg_2Cu phase [22]. As seen in Fig. 6, no peak was observed after 100 h milling time. This may be related to the formation of the solid solution α-Mg(Cu, Y, La).

3.3 The degradation of methyl orange azo dye

For the photocatalytic decomposition experiments of the methyl orange by using the $Mg_{65}Cu_{20}Y_{13}La_2$ powders, the optimization of the concentrations of the dye, catalyst, and $NaBH_4$ was carried out (Fig. 7). In these analyses, 100 ml of dye solution, pH = 6, and 60 min rested time were applied. Thus, the optimum concentrations were determined for the dye, catalyst, and $NaBH_4$ used in the experiments.

Degradation analyses of the methyl orange in dye solutions were examined by absorbance decrease at 465 nm in UV–Vis spectra (Fig. 8). The absorbance at 465 nm is relevant to the azo chromophore group (–N=N–). During the degradation process, the absorbance peak at 465 nm decreases with reductive breakage of the –N=N– group. As shown in Fig. 8, all the $Mg_{65}Cu_{20}Y_{13}La_2$ alloys with 10 h, 50 h, and 100 h milling time effectively degraded the methyl
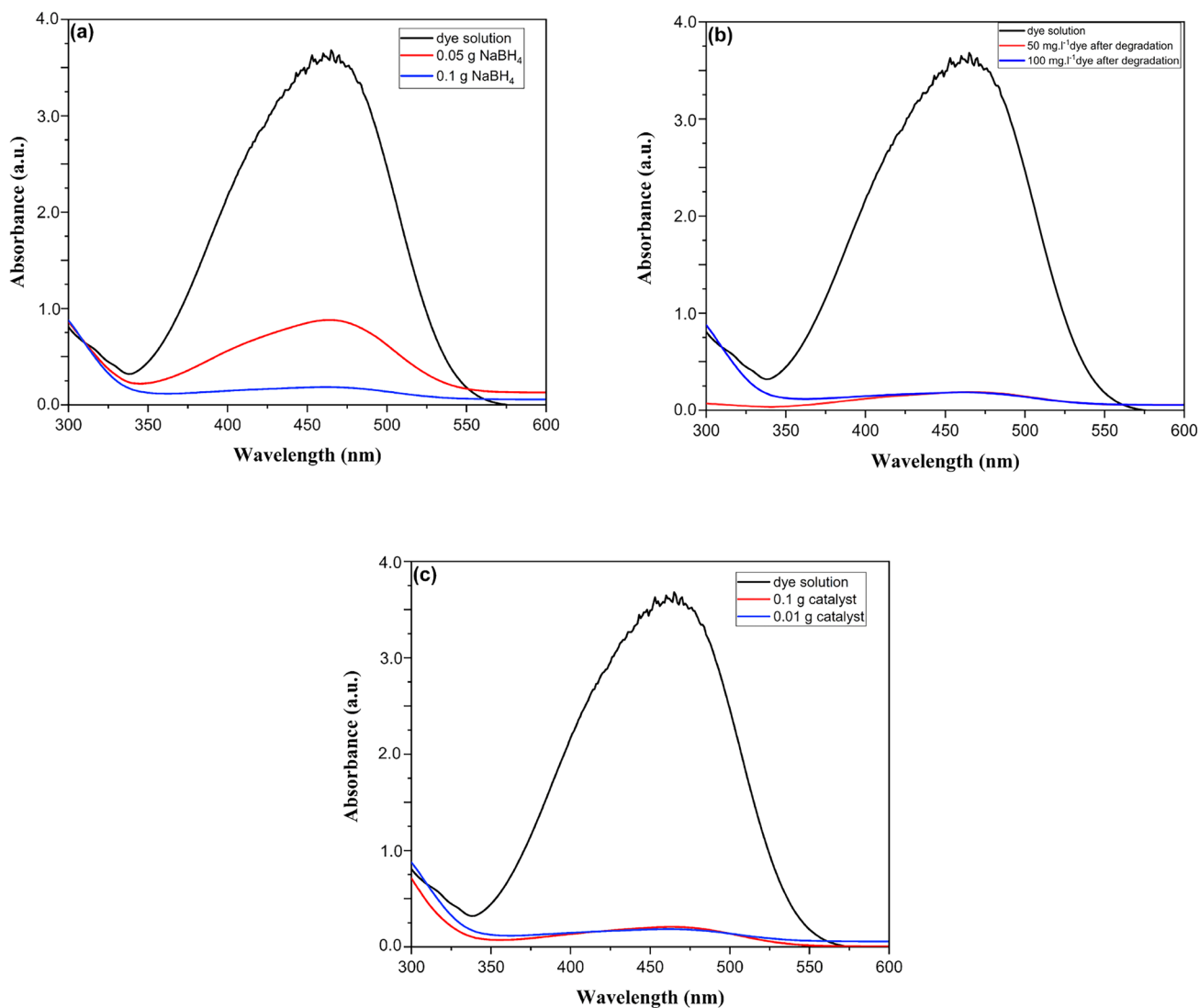
Fig. 7 Concentration optimization of: **a** $NaBH_4$ (0.01 g alloy, 100 mg l^{-1} dye), **b** dye (0.1 g $NaBH_4$, 0.01 g alloy), and **c** catalyst (0.1 g $NaBH_4$, 100 mg l^{-1} dye)

orange. However, the methyl orange degradation rate by using the $Mg_{65}Cu_{20}Y_{13}La_2$ powders for 10 h milling time was lower than that of others (Fig. 8a). This may be due to the refinement of the grains during the ball milling process, which increases the grain boundary area per unit volume [7]. When the milling time increased, the $Mg_{65}Cu_{20}Y_{13}La_2$ alloys with a long milling time caused an increase in dye degradation. This is probably because the synthesized alloys have a larger specific surface area and better surface activity as proven [1]. As shown in Fig. 9, the color of the dye solution turned colorless within 20 min (the $Mg_{65}Cu_{20}Y_{13}La_2$ alloy for 100 h milling time). This shows that the $Mg_{65}Cu_{20}Y_{13}La_2$ alloys could almost

completely degrade methyl orange within 20 min. Minoo Khodamorady et al. [30] showed that BNPs@ $SiO_2(CH_2)_3$–TAPC–$OCH_2CH_2NH_2$–Pd(0) was able to use it as an adsorbent in the removal of methyl orange and methylene blue dyes by using a reducing agent ($NaBH_4$). According to their results, 0.01 g of nanomaterial can degrade dye with 98% efficiency within 40 s for 15 ppm methyl orange concentration. However, in the present study, a higher concentration of the methyl orange (100 ppm) was almost wholly degraded with 94% efficiency for 0.01 g of alloy within 20 min.

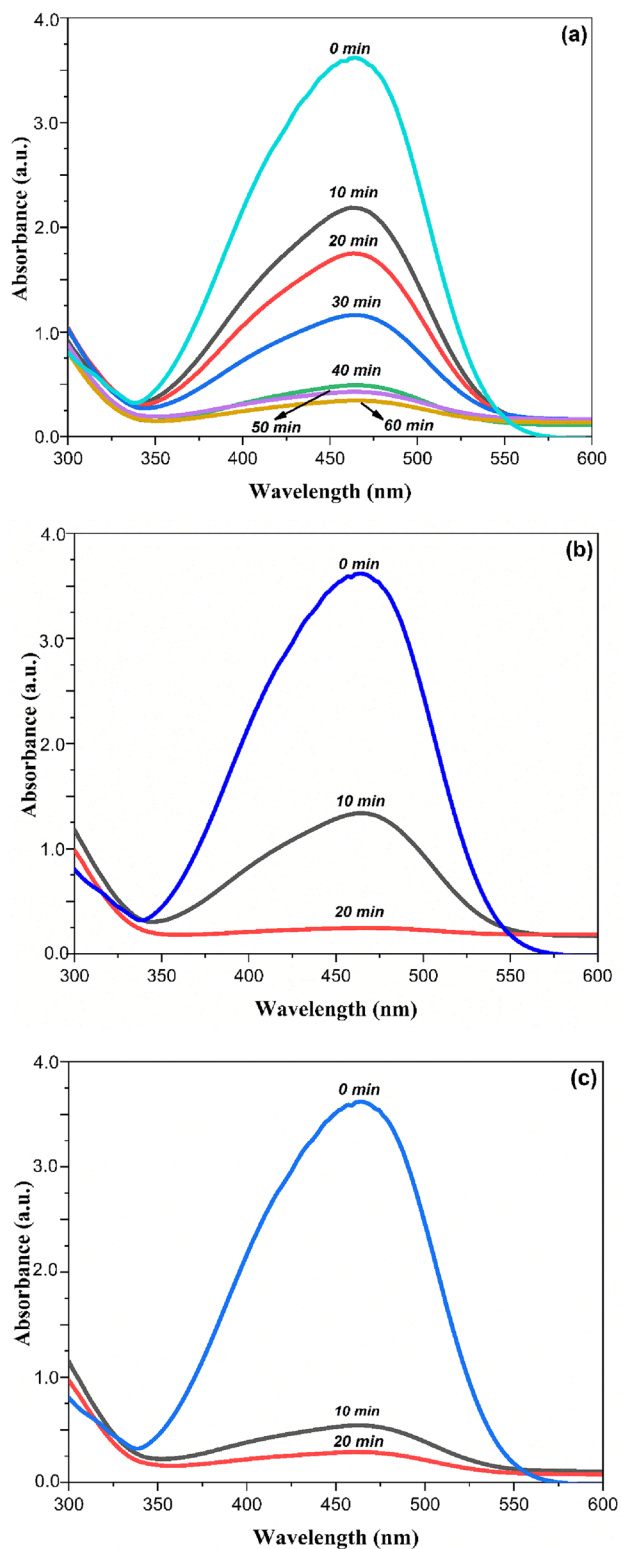In the degradation experiments of the methyl orange, methyl orange did not degrade under the
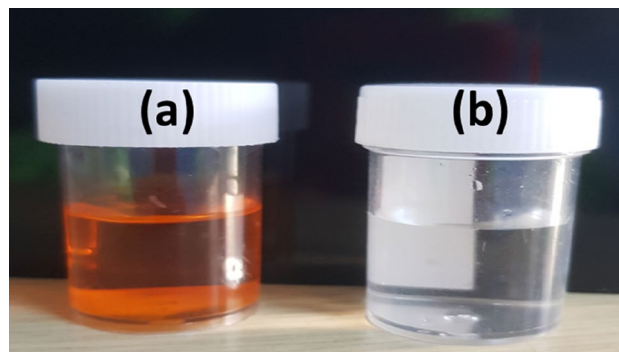
Fig. 9 The color change of dye solution **a** before photocatalytic reaction **b** after photocatalytic reaction

same environmental conditions (pH = 6) without catalysts (Fig. 10). According to the observations of [30], the reducing agent alone ($NaBH_4$) can't remove the methyl orange and this result confirms the current study. It can be said that the $Mg_{65}Cu_{20}Y_{13}La_2$ alloy is very effective in the degradation of the methyl orange. Also, the $Mg_{65}Cu_{20}Y_{13}La_2$ alloy did not show a high yield without the reducing agent ($NaBH_4$) (Fig. 11). $NaBH_4$ is highly accelerated electron transport from the catalyst surface to dye molecules in the catalysis mechanism. Since the dye concentration is directly proportional to the absorbance peak at 465 nm in the removal efficiency calculations, the concentration calculation was made according to the absorbance at different reaction times and converted into removal efficiency. For this, the following equation was used [8].
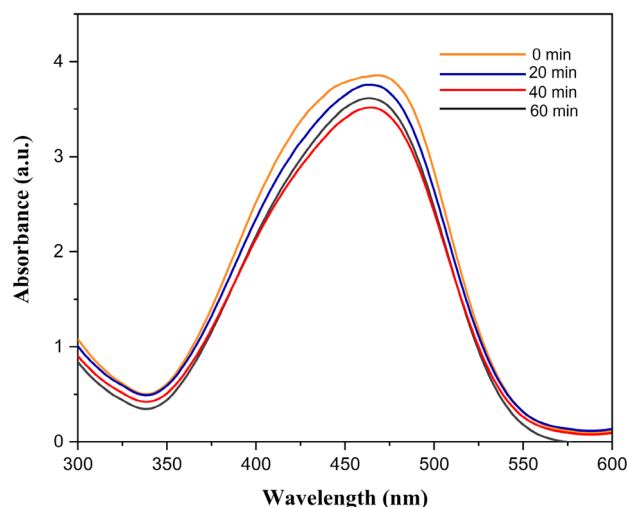

Fig. 8 UV–Vis absorbance spectra of the methyl orange degradation by using the $Mg_{65}Cu_{20}Y_{13}La_2$ alloy for different milling times: **a** 10 h, **b** 50 h, and **c** 100 h

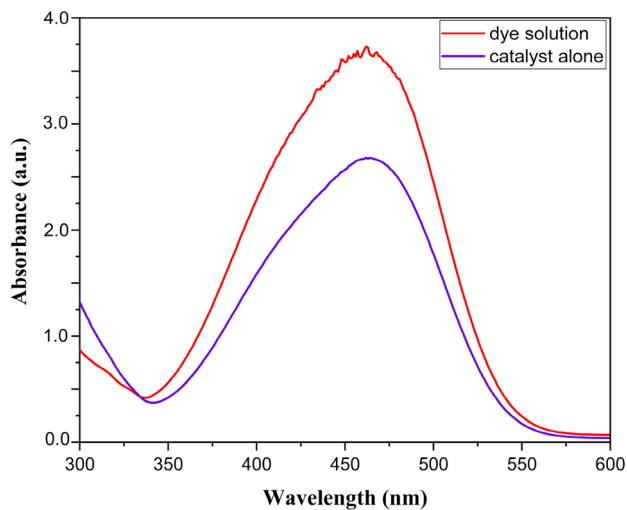**Fig. 10** Degradation efficiency curve without catalyst

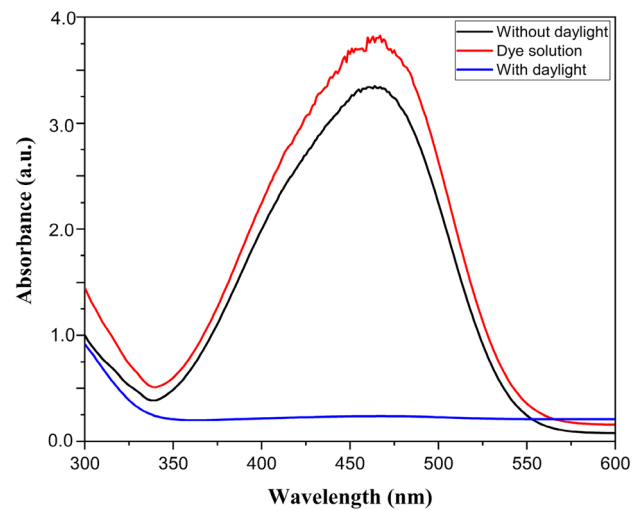**Fig. 11** Degradation efficiency curve without NaBH$_4$ (catalyst alone)

Fig. 12 Degradation efficiency curve without daylight and with daylight

$$\eta = \left[(C_0 - C)/C_0\right] \times 100 \tag{2}$$

where η is the decolorization efficiency (%), C_0 is the initial dye concentration, and C is the dye concentration at the specific reaction time.

The number of electrons emitted by the metal depends on the intensity of the incident light. That is, the number of photoelectrons increases directly proportion with the intensity of the incident light. For this reason, the dye decomposition experiments have been evaluated in both light and non-light environments. For this purpose, dye degradation medium as the same conditions (pH = 6, catalyst amount: 0.01 g, NaBH$_4$: 0.1 g) in the flask was covered with aluminum foil so that it would not receive light. According to UV–Vis analyses, a very small amount of dye removal has been observed in a non-light environment (Fig. 12).

3.3.1 *The effect of pH on the degradation of methyl orange azo dye*

The pH of the dye solution is a critical parameter affecting the removal efficiency. The effect of this factor in determining the degradation ability was analyzed in the pH range of 5–9 . According to Fig. 13, while a high efficiency was achieved in all the pH values studied, the highest efficiency was observed at pH 6. Bowen Z. et al. [17] achieved the highest efficiency for pH 2 in dye degradation by

using CuZr-based catalysts while pH 7 and pH 10 were not achieved. That is, according to their results, the applicable pH range is limited. However, in the current study, a high degradation efficiency from pH 5 to pH 9 has been observed. The high efficiency observed in all the pH values studied has a great importance for wastewater treatment plants because there is no need for additional pH adjustment in wastewater treatment plants, and therefore, it provides advantages such as cost and easy applicability.
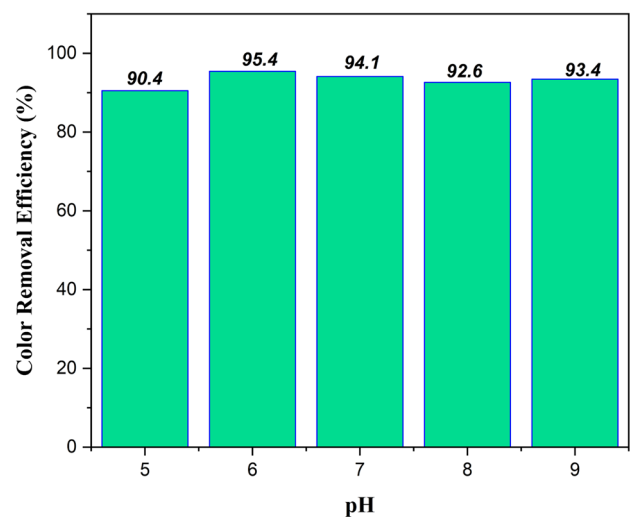

Fig. 13 The effect of pH on the color removal efficiency of the alloy milled for 50 h

3.3.2 FT-IR and GC–MS analysis

FT-IR and GC–MS analyses are essential in determining the characterizations of organic molecules. Thus, since the reaction process can be further understood, FT-IR and GC–MS analyses were examined. According to GC–MS and FT-IR analyses, it is possible to say that the dye samples in the solution are entirely degraded. After the reductive degradation process, the solid was dried and analyzed with FT-IR. The S=O stretches from organic sulfonate groups and aromatic C–N stretches were observed as a broad band at 1320 cm^{-1} in the FT-IR spectrum. In addition, aromatic C=C, C–H bendings, and primary amine N–H wags were recorded at 873 cm^{-1} in the FT-IR spectra after the degradation. Therefore, according to the FT-IR (Fig. 14), it can be said that the methyl orange was degraded with the hydrogenation (reduction) as in the mechanism of the reaction.

In addition, the catalysis medium was dried at 70 °C in an oven. The organic compounds were extracted with absolute ethanol and injected into GC–MS (Fig. 15). According to the GC–MS and FT-IR spectra, it can be said that methyl orange was reductively degraded completely in NaBH$_4$ as a co-factor (Fig. 16). The chromophore groups were degraded and obtained the clear solution after the catalysis. Interestingly, some of the aromatic groups were reductively opened and separated, and some of them were coupled with the other active substituents, as seen in the GC–MS
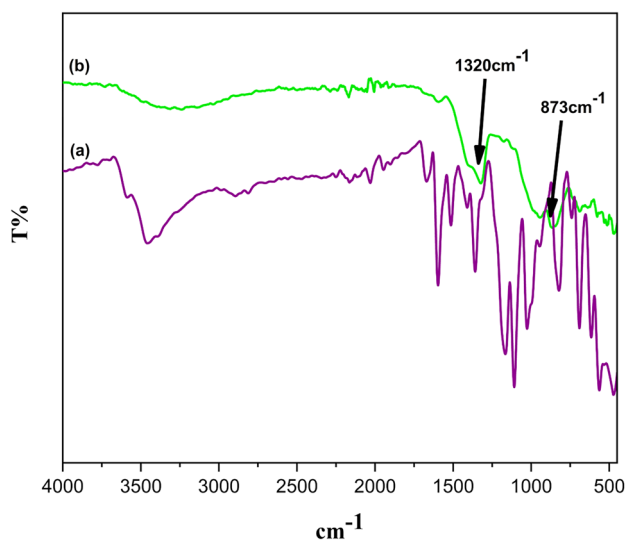

Fig. 14 FT-IR spectra of **a** the methyl orange azo dye and **b** sample after photocatalytic reaction

analysis of the dried and extracted filtrate. Some condensation reactions might arise in the electron impact ionization (EI) source in GC–MS.

Since the methyl orange and the degradation products after catalytic process are as organic compounds, all these compounds can be dissolved in ethanol. Due to the fact that the aqueous product analysis cannot be applied to GC–MS, the final decomposition products, except volatile products, were analyzed by using GC–MS. Also, these decomposition products were characterized and confirmed by FT-IR.

3.3.3 Kinetics of catalytic dye reduction

The linear kinetic behavior in the photocatalytic degradation of the methyl orange by using the Mg$_{65}$Cu$_{20}$Y$_{13}$La$_2$ alloy was examined and calculated as zero-order, pseudo-first-order, second-order, and pseudo-second-order. The reaction rate constants for these processes were obtained as stated in [31]. When the coefficients were calculated, it was seen that the linear kinetic behavior of the methyl orange degradation by using the Mg$_{65}$Cu$_{20}$Y$_{13}$La$_2$ alloy was fitted to the second-order kinetic model with 0.95 (Table 2, Fig. 17).

3.4 Reusability evaluation

Since the adsorption and degradation mechanisms occur on the catalyst's surface, it is essential to study the surface morphology of the alloy to understand the reaction mechanisms [1]. Thus, the surface morphology after the degradation reaction was examined. The original alloy has a homogeneously distributed structure (Fig. 18a). However, it seems that there are particle clusters and inhomogeneous structures after one degradation cycle, according to Fig. 18b. Also, as shown in Fig. 18, some corroded pits [1] on the alloy surface and reagglomeration [32] after degradation appear, so corroded pits may be caused by surface passivation. The surface passivation can affect the reusability of the alloy, which is an essential factor for industrial applications. Tang et al. have stated that the corrosion products formed in the alloy surface after the degradation reaction of azo dye may cause surface passivation [14]. XPS was used to investigate the distribution of elements on the alloy surface after degradation. Figure 19 shows the XPS full spectrum of corresponding elements
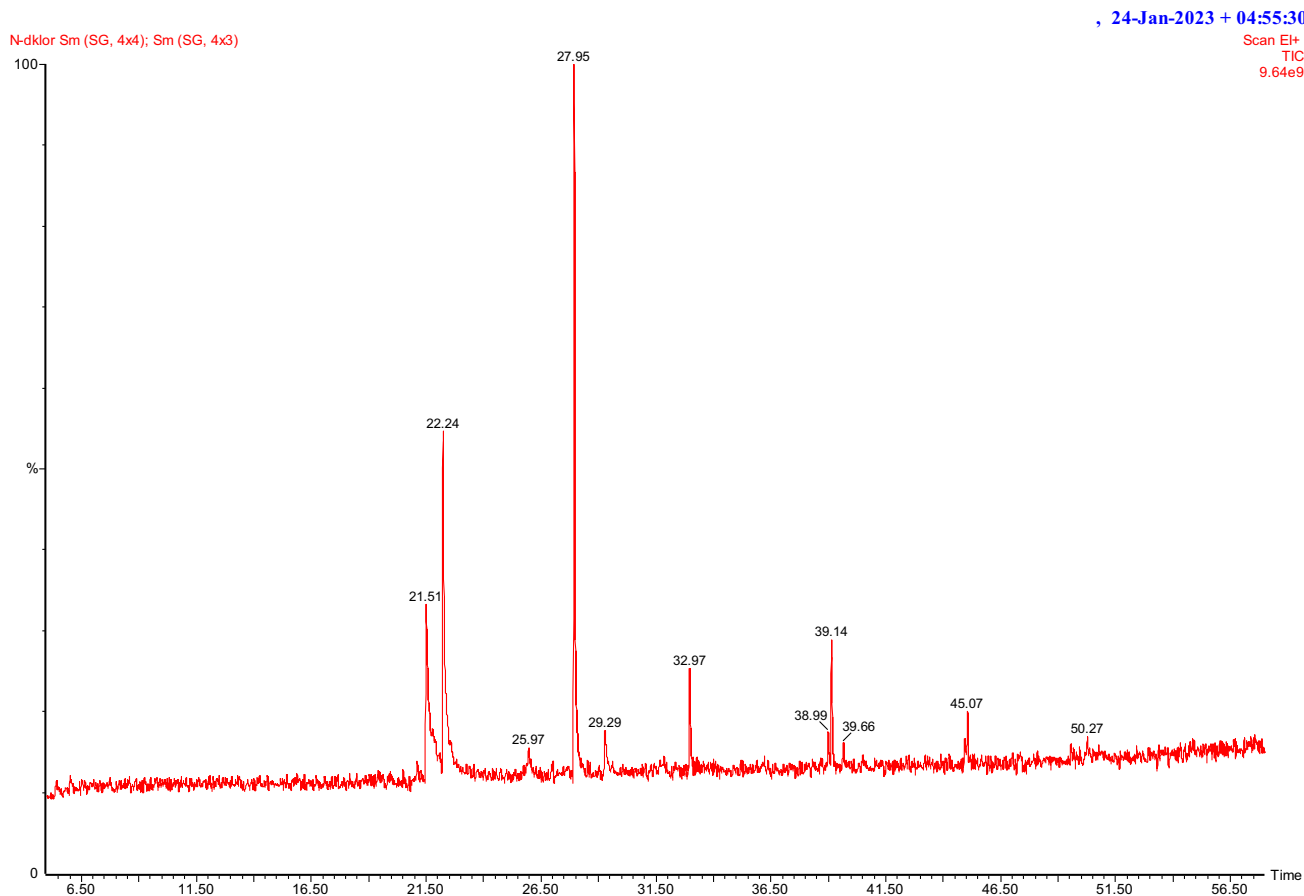
Fig. 15 GC–MS chromatogram of the liquid phase of the catalysis

after the degradation of the sample. While the Mg, Cu, and Y elements are present in the sample, the O element is associated with the advanced oxidation process. In addition, the C element seen in Fig. 19 comes from azo dye [14].

The reusability of catalysts is a significant factor in industrial applications [1]. In present reusability evaluation as seen in Fig. 20, the performance of the $Mg_{65}Cu_{20}Y_{13}La_2$ alloy was noticeable although there is a low number of repeated cycles of Mg-based alloys as stated in [14]. According to Fig. 20, it was observed that the color removal efficiency of methyl orange solution did not change much and remained above 91% after the four times repeated uses, but a sharp decrease was observed as increased to fifth cycle. This is probably due to the surface structure of the alloy, which provides more active sites in the degradation reaction. As stated in Ma et al. [1], it is possible to assume that the alloy surface is covered with degradation products.

4 Conclusions

In summary, the current study examined the effect of milling time on the microstructure of the $Mg_{65}Cu_{20}Y_{13}La_2$ alloy and on the azo dye methyl orange degradation by using the $Mg_{65}Cu_{20}Y_{13}La_2$ alloy synthesized by the MA method under an argon gas atmosphere. After MA process with 10 h milling time, $Mg_{24}Y_5$, Mg_2Cu, and Mg_2Cu_2La phases were formed. However, after 100 h milling time, single-phase solid solution α-Mg(Cu, Y, La) was formed, which indicates that the ball milling time during MA is an important factor. The crystallite size was determined as 21 nm after 100 h milling time. Phase transformations in the alloys were determined by the DSC curves. It was concluded that exothermic peaks that occur after 10 h milling time may be attributed to the formation of the $Mg_{24}Y_5$ and Mg_2Cu phases and the absence of any peaks after 100 h milling time may be attributed to the formation of α Mg(Cu, Y, La) solid solution. The $Mg_{65}Cu_{20}Y_{13}La_2$ alloy was not only

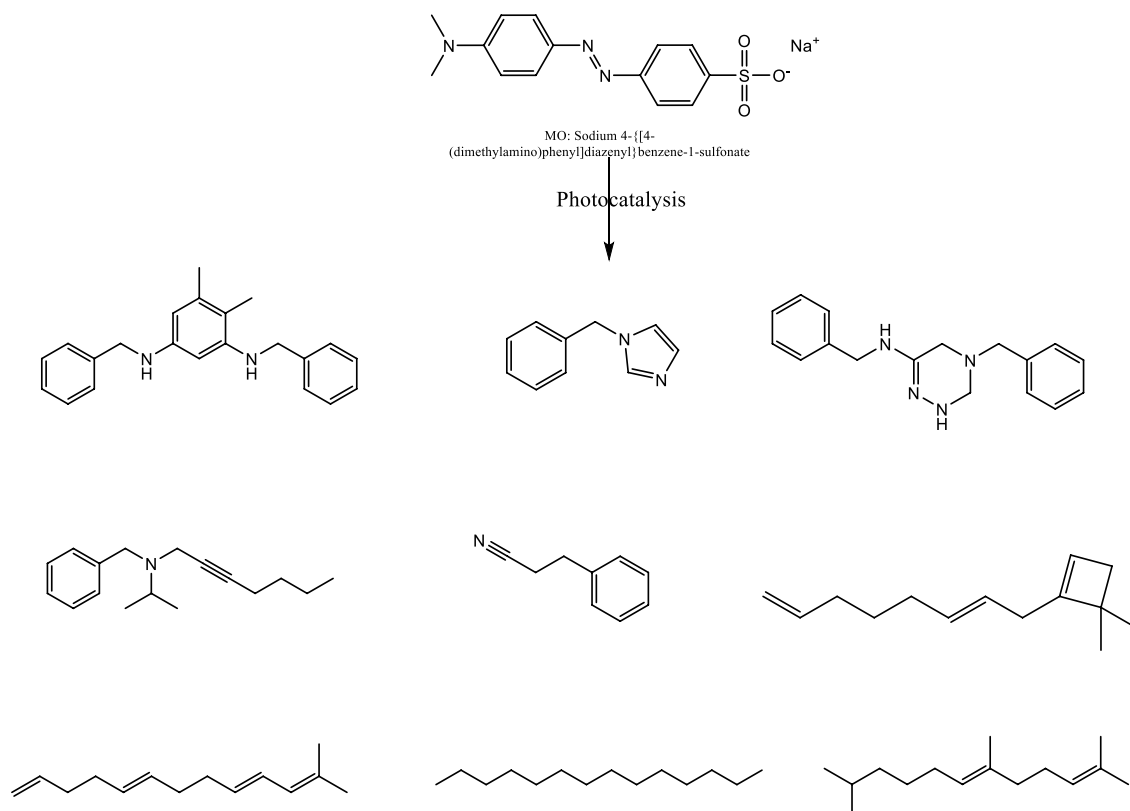MO: Sodium 4-{[4-(dimethylamino)phenyl]diazenyl}benzene-1-sulfonate

Photocatalysis

Fig. 16 Possible reductive degradation products evaluated GC–MS spectrum and library search in ethanol extract of the dried form of the liquid phase

Table 2 Kinetic models

Model	Equation	k (min^{-1})	R^2	Model	Equation	k (min^{-1})	R^2
Zero-order	$C - C_0 = -kt$	72.47	0.73	Second-order	$1/C - 1/C_0 = kt$	0.04	0.95
Pseudo-first-order	$\ln (C/C_0) = -kt$	0.19	0.94	Pseudo-second-order	$t/C = t/C_0 - 1/kC_0^2$	4.71	0.87

determined by having good the methyl orange degradation within a short time (20 min), but also had applicable wide pH range and four-cycle reusability. The current study provides an advantage with degradation of the high dye concentration (100 ppm). Moreover, the decomposition reaction mechanism of the methyl orange by using the $Mg_{65}Cu_{20}Y_{13}La_2$ alloy offers a different perspective on the subject.
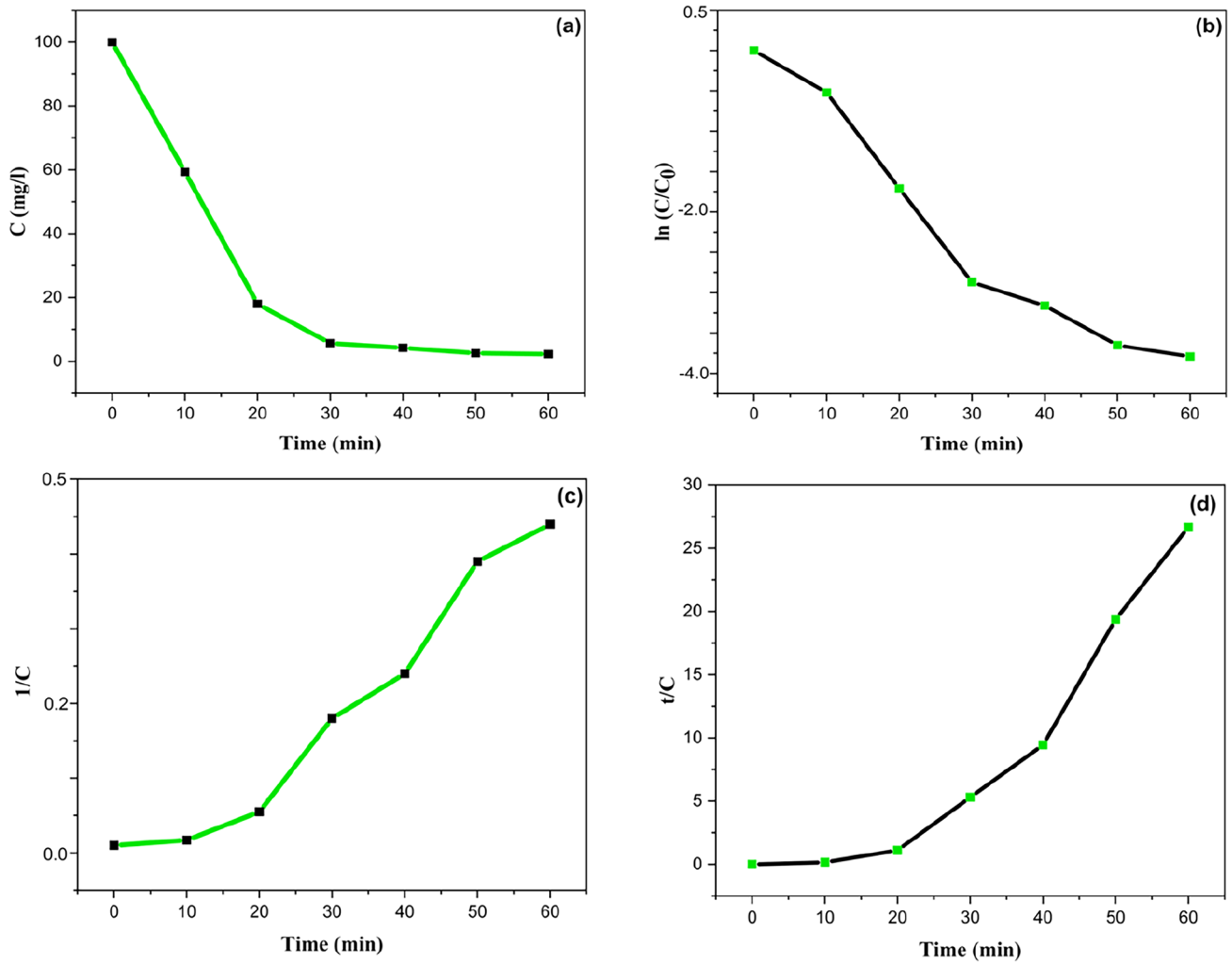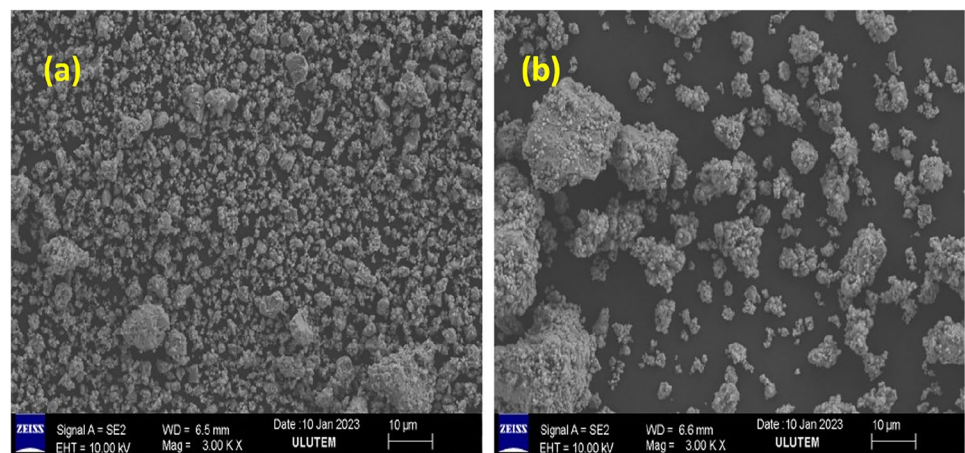
Fig. 17 Compared reaction linear kinetic models for the photocatalytic degradation of the methyl orange by using the $Mg_{65}Cu_{20}Y_{13}La_2$ alloy milled for 50 h: **a** zero-order, **b** pseudo-first-order, **c** second-order, **d** pseudo-second-order

Fig. 18 SEM images of the $Mg_{65}Cu_{20}Y_{13}La_2$ alloy for 100 h milling time. **a** Origin, **b** after 1 degradation cycle
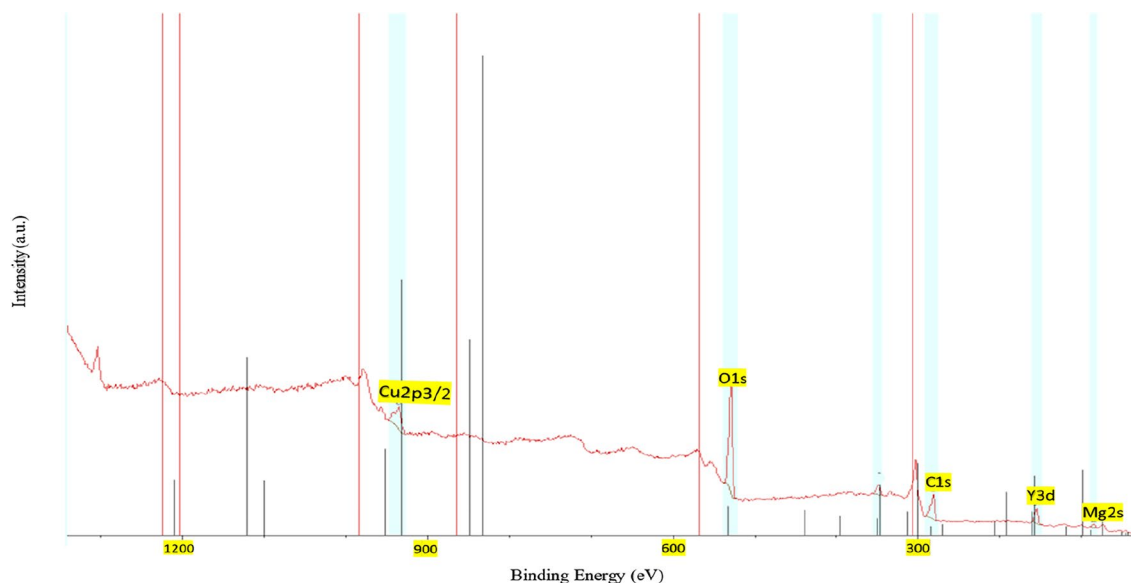
Fig. 19 XPS spectra of the $Mg_{65}Cu_{20}Y_{13}La_2$ alloy for 100 h milling time after 1 degradation cycle
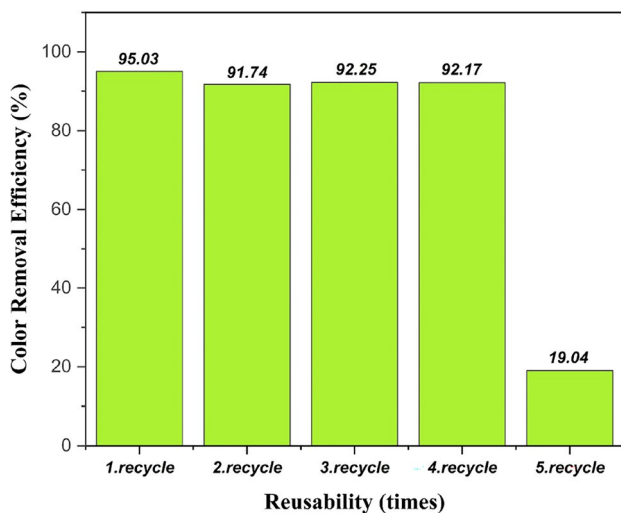

Fig. 20 Reusability of the $Mg_{65}Cu_{20}Y_{13}La_2$ catalyst (for 100 h milling time) for the methyl orange degradation (pH = 6)

Author contributions

All authors contributed to the study conception and design. Material preparation, data collection, and analysis were performed by Nilüfer Danacı. The first draft of the manuscript was written by Musa Göğebakan and all authors commented on the previous versions of the manuscript. All authors read and approved the final manuscript.

Funding

Acknowledgements

Data availability

The data that support the findings of this study are available from the corresponding author (Nilüfer Danacı) upon reasonable request.

Declarations

Conflict of interest All authors certify that they have no affiliations with or involvement in any organization or entity with any financial interest or nonfinancial interest in the subject matter or materials discussed in this manuscript.

References

1. Y. Ma, L. Xie, Q. Li, C. Chang, H. Li, B. Mu, X. Ma, Influence of surface morphology of Fe-based amorphous alloys on the degradation of an azo dye. J. Phys. Chem. Solids **163**, 110596 (2022)

2. C. Zhang, Z. Zhu, H. Zhang, Mg-based amorphous alloys for decolorization of azo dye. Results Phys. **7**, 2054–2056 (2017)

3. F.X. Deng, J.X. Yang, Y.S. Zhu, F. Ma, S. Qiu, A rapid azo dye decolorization of methyl orange by the foam zerovalent nickel. Environ. Prog. Sustain. Energy **37**, 686–694 (2018)

4. S. Nam, P.G. Tratnyek, Reduction of azo dyes with zerovalent iron. Water Res. **34**, 1837–1845 (2000)

5. C.D. Raman, S. Kanmani, Textile dye degradation using nano zero valent iron: a review. J. Environ. Manag. **177**, 341–355 (2016)

6. M. AboliGhasemabadi, W.B. Mbarek, A. Cerrillo-Gil, H. Roca-Bisbe, O. Casabella, P. Blanquez, E. Pineda, L. Escoda, J.J. Sunol, Azo-dye degradation by Mn–Al powders. J. Environ. Manag. **258**, 110012 (2020)

7. C. Suryanarayana, Mechanical alloying and milling (review). Prog. Mater. Sci. **46**, 1–184 (2001)

8. S. Chen, N. Chen, M. Cheng, S. Luo, Y. Shao, K. Yao, Multi-phase nanocrystallization induced fast degradation of methyl orange by annealing Fe-based amorphous ribbons. Intermetallics **90**, 30–35 (2017)

9. C. Zhang, H. Zhang, M. Lv, Z. Hu, Decolorization of azo dye solution by Fe–Mo–Si–B amorphous alloy. J. Non Cryst. Solids **356**, 1703–1706 (2010)

10. A. Lassoued, J.F. Li, Influence of iron content in Fe-based amorphous alloy catalysts on degradation of azo dyes by fenton-like process. J. Phys. Chem. Solids **180**, 111475 (2023)

11. J.Q. Wang, Y.H. Liu, M.W. Chen, D.V. Louzguine-Luzgin, A. Inoue, J.H. Perepezko, Excellent capability in degrading azo dyes by MgZn-based metallic glass powders. Sci. Rep. **2**, 418 (2012)

12. K.W. Jung, B.H. Choi, C.M. Dao, Y.J. Lee, J.W. Choi, K.H. Ahn, S.H. Lee, Aluminum carboxylate-based metal-organic frameworks for effective adsorption of anionic azo dyes from aqueous media. J. Ind. Eng. Chem. **59**, 149–159 (2018)

13. X.D. Qin, Z.W. Zhu, G. Liu, H.M. Fu, H.W. Zhang, A.M. Wang, H. Li, H.F. Zhang, Ultrafast degradation of azo dyes catalyzed by cobalt-based metallic glass. Sci. Rep. **5**, 18226 (2016)

14. M. Tang, L. Lai, D. Ding, T. Liu, W. Kang, N. Guo, B. Song, S. Guo, Rapid degradation of direct blue dye by Co-based amorphous alloy wire. J. Non Cryst. Solids **576**, 121282 (2022)

15. Z. Lv, Y. Yan, C. Yuan, B. Huang, C. Yang, J. Ma, J. Wang, L. Huo, Z. Cui, X. Wang, W. Wang, B. Shen, Making Fe-Si-B amorphous powders as an effective catalyst for dye degradation by high-energy ultrasonic vibration. Mater. Des. **194**, 108876 (2020)

16. L.C. Zhang, Z. Jia, F. Lyu, S.X. Liang, J. Lu, A review of catalytic performance of metallic glasses in wastewater treatment: recent progress and prospects. Prog. Mater. Sci. **105**, 100576 (2019)

17. B. Zhao, Z. Zhu, X.D. Qin, Z. Li, H. Zhang, Highly efficient and stable CuZr-based metallic glassy catalysts for azo dye degradation. J. Mater. Sci. Technol. **46**, 88–97 (2020)

18. L. Ji, S.Y. Peng, Z.G. Zheng, J.L. Zuo, D.C. Zeng, Z.G. Qiu, M. Xiao, J.W. Chen, H.Y. Yu, The degradation performance of the $Fe_{78}Si_{13}B_9$ and $(FeCoNi)_{78}Si_{13}B_9$ high-entropy amorphous alloy ribbons. J. Alloys Compd. **815**, 152347 (2020)

19. C. Kursun, M. Gogebakan, H. Eskalen, S. Urus, J.H. Perepezko, Microstructural evaluation and highly efficient

photocatalytic degradation characteristic of nanostructured $Mg_{65}Ni_{20}Y_{15-x}La_x$(x=1,2,3) alloys. J. Inorg. Organomet. Polym. Mater. **30**, 494–503 (2020)

20. Q. Chen, Z. Yan, L. Guo, H. Zhang, K. Kim, X. Li, W. Wang, Enhancing the acid orange dye degradation efficiency of Mg-based glassy alloys with introducing porous structure and zinc oxide. J. Alloys Compd. **831**, 154817 (2020)

21. A. Amri, L. Kadiri, R. Hsissou, A. Lebkiri, Z. Wardighi, E.H. Rifi, A. Lebkiri, Investigation of Typha Latifolia (TL) as a potential biosorbent for removal of the methyl orange anionic dye in the aqueous solution. Kinetic and DFT approaches. J. Mol. Struct. **1272**, 134098 (2023)

22. C. Martínez, S. Ordoñez, D. Guzmán, D. Serafini, I. Iturriza, O. Bustos, Phase evolution and thermal stability of 2 Mg–Cu alloys processed by mechanical alloying. J. Alloys Compd. **581**, 241–245 (2013)

23. H. Yu, X.R. Dong, S.M. Kang, W. Yu, Z.F. Wang, J.Y. Mu, X.W. Cui, J.H. Li, F.X. Yin, K.S. Shin, Effect of the pre-homogenization on the precipitation behaviors, mechanical and corrosion properties of as-extruded Mg–Y binary alloys. Mater Charact **178**, 111307 (2021)

24. C. Suryanarayana, M.G. Norton, *X-rays and Diffraction* (Springer, Cham, 1998)

25. C. Kursun, M. Gogebakan, Characterization of nanostructured Mg–Cu–Ni powders prepared by mechanical alloying. J. Alloys Compd. **619**, 138–144 (2015)

26. A. Azimi, A. Shokuhfar, A. Zolriasatein, Nanostructured Al–Zn–Mg–Cu–Zr alloy prepared by mechanical alloying followed by hot pressing. Mater. Sci. Eng. A **595**, 124–130 (2014)

27. M. Gogebakan, C. Kursun, J. Eckert, Formation of new Cu-based nanocrystalline powders by mechanical alloying technique. Powder Technol. **247**, 172–177 (2013)

28. M. Wang, H. Sun, B. Pang, X. Xi, Z. Nie, Structure evolution of Y_2O_3 and consequent effects on mechanical properties of W-Y_2O_3 alloy prepared by ball milling and SPS. Mater. Sci. Eng. A **832**, 142448 (2022)

29. H. Yaykaşlı, H. Eskalen, Y. Kavun, M. Gögebakan, Microstructural, thermal, and radiation shielding properties of $Al_{50}B_{25}Mg_{25}$ alloy prepared by mechanical alloying. J. Mater. Sci. Mater. Electron. **33**, 2350–2359 (2022)

30. M. Khodamorady, M. Jafarzadeh, K. Bahrami, Design and introduction of BNPs@ SiO_2 (CH2)3-TAPC-O-(CH2) 2NH2-Pd (0) as an efficient nano-catalyst for the coupling reactions and removing of organic dyes. Inorg. Chem. Commun. **148**, 110290 (2023)

31. S. Uruş, M. Çaylar, H. Eskalen, Ş Özgan, Synthesis of GO@ Fe_3O_4@ TiO_2 type organic–inorganic nanohybrid material: investigation of the effect of nanohybrid doped liquid crystal E7 and the photocatalytic degradation of cirofloxacin. J. Mater. Sci. Mater. Electron. **33**, 4314–4329 (2022)

32. M. Ramya, M. Karthika, R. Selvakumar, B. Raj, K.R. Ravi, A facile and efficient single step ball milling process for synthesis of partially amorphous Mg–Zn–Ca alloy powders for dye degradation. J. Alloys Compd. **696**, 185–192 (2017)

33. R.H. Petrucci, F.G. Herring, J.D. Madura, C. Bissonnette, *Genel Chemistry Principles and Modern Applications*, 11th edn. (Pearson, Toronto, 2017), p.309

Publisher's Note   Springer Nature remains neutral with regard to jurisdictional claims in published maps and institutional affiliations.